



# Intercritical annealing to achieve a positive strain-rate sensitivity of mechanical properties and suppression of macroscopic plastic instabilities in multi-phase medium-Mn steels

J.T. Benzing<sup>a,b,\*</sup>, W.E. Luecke<sup>c</sup>, S.P. Mates<sup>c</sup>, D. Ponge<sup>d</sup>, D. Raabe<sup>d</sup>, J.E. Wittig<sup>a</sup>

<sup>a</sup> Interdisciplinary Materials Science, Vanderbilt University, Nashville, TN, 37235-1683, USA

<sup>b</sup> National Institute of Standards and Technology, Applied Chemicals and Materials Division, 325 Broadway, Stop 647, Boulder, CO, 80305, USA

<sup>c</sup> National Institute of Standards and Technology, Materials Science and Engineering Division, 100 Bureau Drive, Stop 8553, Gaithersburg, MD, 20899, USA

<sup>d</sup> Max-Planck-Institut für Eisenforschung, Max-Planck-Str. 1, 40237, Düsseldorf, Germany

## ARTICLE INFO

### Keywords:

Medium-Mn steel  
Multi-phase steel  
Positive strain-rate sensitivity  
Servo hydraulic tension  
Kolsky bar tension

## ABSTRACT

This study investigates the high strain-rate tensile properties of a cold-rolled medium-Mn steel (Fe–12Mn–3Al–0.05C % in mass fraction) designed to have a multi-phase microstructure and positive strain-rate sensitivity. At the intercritical annealing temperature of 585 °C, increasing the annealing time from 0.5 h to 8 h increased the phase volume fraction of ultrafine-grained (UFG) austenite from 2% to 35% by reversion. The remainder of the microstructure was composed of UFG ferrite and recovered  $\alpha'$ -martensite (the latter resembles the cold-rolled state). Servo hydraulic tension testing and Kolsky-bar tension testing were used to measure the tensile properties from quasi-static strain rates to dynamic strain rates ( $\dot{\epsilon} = 10^{-4} \text{ s}^{-1}$  to  $\dot{\epsilon} = 10^3 \text{ s}^{-1}$ ). The strain-rate sensitivities of the yield strength (YS) and ultimate tensile strength (UTS) were positive for both annealing times. Tensile properties and all non-contact imaging modalities (infrared imaging and digital image correlation) indicated an advantageous suppression of Lüders bands and Portevin Le Chatelier (PLC) bands (a critical challenge in multi-phase medium-Mn steel design) due to the unique combination of microstructural constituents and overall composition. Fracture surfaces of specimens annealed for 0.5 h showed some instances of localized cleavage fracture (approximately 30  $\mu\text{m}$  wide areas and lath-like ridges). Specimens annealed for 8 h maintained a greater product of strength and elongation by at least 2.5 GPa % (on average for each strain rate). The relevant processing-structure-property relationships are discussed in the context of recommendations for design strategies concerning multi-phase steels such that homogeneous deformation behavior and positive strain-rate sensitivities can be achieved.

## 1. Introduction

Multi-phase medium-Mn steels can be produced with simple processing steps and moderate alloying content to balance manufacturing cost and desired mechanical properties for automotive applications [1–5]. Desirable characteristics of next-generation advanced high-strength steels (AHSS) include a multi-phase microstructure, moderate alloying content (less than 15% mass fraction), and products of strength and elongation totaling 30 GPa% or more [1,2,6–8]. One class of AHSS that may satisfy these requirements is referred to as medium-Mn steel. Cold rolling of medium-Mn steel produces a deformed martensitic microstructure [9,10], and subsequent intercritical annealing yields small grains of austenite and ferrite on the order of a few

hundred nanometers in diameter [11,12]. The intercritical annealing step also determines the austenite stacking fault energy, which influences the strain hardening behavior through transformation- and twinning-induced plasticity (TRIP and TWIP) effects [12–17].

A challenge with exploring new chemical compositions of multi-phase steels is suppressing static and dynamic strain aging effects, such as Lüders bands, Portevin-Le Chatelier (PLC) bands, and serrated flow stress patterns [18–23]. These static and dynamic strain aging events can lead to unstable plastic deformation behavior (non-uniformity and/or strain localization). Specifically, unstable material flow stresses during sheet forming processes pose significant challenges for automotive applications, including premature ductile fracture from a decrease in the amount of post-uniform elongation [24,25]. Optimizing

\* Corresponding author. Interdisciplinary Materials Science, Vanderbilt University, Nashville, TN, 37235-1683, USA.

E-mail address: [jake.benzing@nist.gov](mailto:jake.benzing@nist.gov) (J.T. Benzing).

a material for sheet forming also requires consideration of strain-rate sensitivity. Medium-Mn steels that exhibit a decrease in ultimate tensile strength (UTS) as strain-rate increases (negative strain-rate sensitivity) usually exhibit strain aging effects, large elongations, and significant rises in specimen temperature during deformation. Therefore, implementation of medium-Mn steels into the automotive industry, with respect to rapid forming operations and crash-safety standards, necessitates a better understanding of the high strain-rate behavior, specifically in the strain-rate ( $\dot{\epsilon}$ ) range from  $\dot{\epsilon} = 10^{-2} \text{ s}^{-1}$  to  $\dot{\epsilon} = 10^3 \text{ s}^{-1}$  [26–28].

This study focuses on a specific steel composition and heat treatment temperature that includes ultrafine-grained (UFG) austenite with a room temperature (RT) stacking-fault energy (SFE) of  $21 \text{ mJ/m}^2$  [29]. The purpose of embedding this type of austenite in a multi-phase microstructure harnesses advantageous effects on strain hardening through mechanical twinning and  $\epsilon$ -martensite formation in the same grain (a balance in mechanical stability/transformation behavior) [3,30–40]. A previous work [29] quantified the compositions of austenite, and most grains observed for the 0.5 h and 8 h annealing times (heat treated at  $585 \text{ }^\circ\text{C}$ ) matched what was predicted based on thermodynamic simulations using Thermo-Calc. In other recent work [41], the intended deformation mechanisms (TWIP and some TRIP effects) were observed in specimens annealed for 8 h and in samples deformed across a large range of strain rates (from  $\dot{\epsilon} = 10^{-4} \text{ s}^{-1}$  to  $\dot{\epsilon} = 10^1 \text{ s}^{-1}$ ). In the current work, tensile properties of the 0.5 h heat treatment were measured with servo hydraulic and Kolsky bar tension testing using a wider range of strain rates (from  $\dot{\epsilon} = 10^{-4} \text{ s}^{-1}$  to  $\dot{\epsilon} = 10^3 \text{ s}^{-1}$ ). The Kolsky bar testing required a different specimen geometry, so results from servo hydraulic and Kolsky bar testing are only directly compared until the end of uniform elongation. To give greater context, the 0.5 h and 8 h heat treatments are compared and analyzed in greater detail. Based on a combination of characterization techniques electron backscatter diffraction (EBSD), digital image correlation (DIC), thermal imaging and fractography, the effects of annealing time and strain rate on structure-property relationships were investigated for the low-C medium-Mn steel. In particular, the variation in morphology (equiaxed, rod-like and plate-like) of the UFG phases, plus a large fraction of recovered  $\alpha'$ -martensite, translate to an increase in yield strength and product of UTS and uniform elongation as strain rate increases. Another advantage of the multi-phase microstructure that contains recovered  $\alpha'$ -martensite as a main constituent is the absence of discontinuous yielding and dynamic strain aging during tensile deformation at all strain rates. Moreover, investigating the relationships between microstructure and mechanical properties under high-strain-rate conditions will be useful in advancing the design of more multi-phase AHSS and predicting performance in extreme loading conditions.

## 2. Experimental methods

### 2.1. Material

After arc melting, a slab of Fe–12Mn–3Al–0.05C (% mass fraction) was subjected to hot rolling ( $900 \text{ }^\circ\text{C}$ ), homogenization ( $1100 \text{ }^\circ\text{C}$  for 2 h in an Ar environment), and a water quench to room temperature (below the  $M_s$  temperature). Subsequent cold rolling (50% thickness reduction) created a completely martensitic steel sheet with a thickness of 1.7 mm. After removal of a thin oxide scale via parallel plate grinding, the final sheet thickness was 1.4 mm. Optical micrographs of the cold-rolled

material (mostly  $\alpha'$ -martensite) are shown in the supplementary material. Thermo-Calc<sup>1</sup> simulations guided the choice of intercritical annealing temperature ( $585 \text{ }^\circ\text{C}$ ), as detailed in Ref. [29]. Composition of the annealed specimens (annealing times of 0.5 h and 8 h) were analyzed by a third-party using X-ray fluorescence and furnace combustion, shown in Table 1.

### 2.2. Microstructural characterization after annealing

Samples of the annealed material were prepared for characterization by mounting, grinding (SiC paper), and polishing (diamond suspension and 50 nm silica). EBSD scans were performed using a 30 nm step size in a field emission scanning electron microscope (FE-SEM) with an accelerating voltage of 15 keV.

### 2.3. Mechanical test setup and non-contact measurements

Tensile specimens were machined from the steel sheets (water jetting) and polished. Full-thickness (1.4 mm) sheet tensile specimens were machined with the tensile direction parallel to the rolling direction. The reduced gauge section used in servo hydraulic tension testing was  $25 \text{ mm} \times 6 \text{ mm}$  and the reduced gauge section for Kolsky bar tensile specimens was  $6.9 \text{ mm} \times 3 \text{ mm}$ . Drawings for the machined tensile specimens are shown in the supplementary material. Parameters governing data acquisition, servo hydraulic tension testing (from  $\dot{\epsilon} = 10^{-4} \text{ s}^{-1}$  to  $\dot{\epsilon} = 10^2 \text{ s}^{-1}$ ), infrared imaging, and DIC conditions for this strain rate range are consistent with reference [41]. Forces in the highest rate servo hydraulic test ( $\dot{\epsilon} = 2 \times 10^2 \text{ s}^{-1}$ ) were measured using two strain gauges mounted on opposite sides of the upper head of the specimens. The gauges were calibrated in situ before each test against the piezoelectric load cell. Tension tests conducted at approximately  $\dot{\epsilon} = 10^3 \text{ s}^{-1}$  used a direct-tension Kolsky bar system with a 1 m striker bar. Lighting during DIC measurements incorporates a triggered flash (1  $\mu\text{s}$  shutter) and images are recorded at  $7.5 \times 10^4$  frames per second with a Photron SA1 camera (128 pixels  $\times$  352 pixels in the gauge section). The Kolsky bar apparatus is shown schematically in the supplementary material and is based on a design from Ref. [42] to simplify the use of pulse-shaping and decrease oscillation amplitude directed by the incident pulse. Kolsky bar specimens were pin-loaded into the Kolsky bar apparatus using press-fit hardened steel pins. Pull-to-failure Kolsky bar tests were conducted with a striker bar speed of approximately  $11.25 \text{ m s}^{-1} \pm 0.25 \text{ m s}^{-1}$  (measured with a laser sensor). Stress data were obtained from the transmitted strain gauge-time signal while the strain data were determined from the average strain (from DIC) obtained over the gauge section. The uncertainty in the stress measurements are  $\pm 4\%$  (estimated from standard error propagation techniques).

### 2.4. Fractography and inclusion analysis

Secondary electron images were recorded from areas of interest on fracture surfaces using a FE-SEM (25 keV). Compositional measurements of various particles observed on fracture surfaces were performed using energy dispersive spectroscopy (EDS) and are shown in the supplementary material. AZtec software (Oxford Instruments) was used to record and analyze the EDS spectra.

<sup>1</sup> Certain commercial software, equipment, instruments or materials are identified in this paper in order to specify the experimental procedure adequately. Such identification is not intended to imply recommendation or endorsement by the National Institute of Standards and Technology, nor is it intended to imply that the equipment or materials identified are necessarily the best available for the purpose.

**Table 1**  
Steel sheet composition after processing and heat treatment.

Element	Fe	Mn	Al	C	Si	Ni	S	N	P	O
mass fraction (%)	balance	12.27	3.01	0.046	<0.1	0.069	0.006	0.002	<0.01	0.0012

### 3. Results

#### 3.1. Microstructure measurements after intercritical annealing

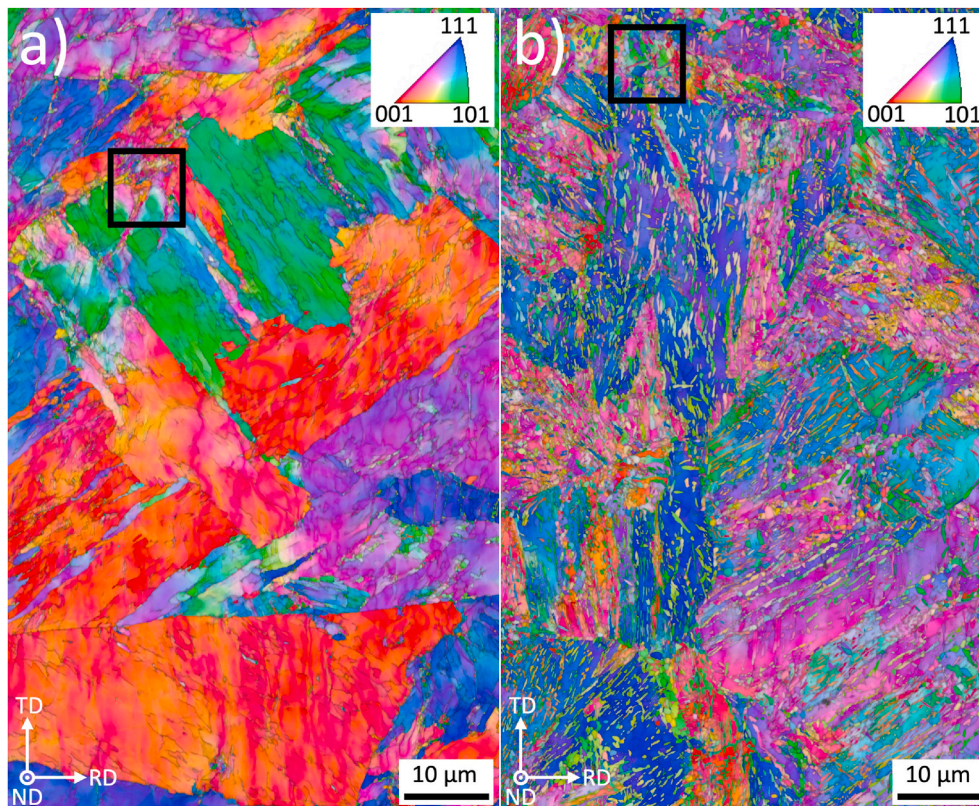
Fig. 1 shows grain orientation maps of medium-Mn steel for both annealing times, where RD indicates rolling direction, TD stands for transverse direction, and ND is the normal direction. After annealing for 0.5 h, the population of UFG austenite (from reversion) was heterogeneously dispersed throughout the recovered martensitic microstructure (Fig. 1a) and comprised 2% of the total area. Fig. 2a/c reveals some ultra-fine ferrite grains and ultrafine austenite grains (encompassed by a recovered  $\alpha'$ -martensitic matrix). The recovered martensite (coarse-grained regions that have not reverted to UFG austenite, nor recrystallized to UFG ferrite) bears a strong resemblance to the cold-rolled material (deformed  $\alpha'$ -martensite) even after 8 h of annealing (Fig. 1b). An increase in annealing time (from 0.5 h to 8 h) increases the austenite content to 35% and increases the austenite grain size, with most of the UFG austenite dispersed nearly homogeneously throughout the microstructure. Notably, austenite grains in the 8 h annealing condition vary in morphology (equiaxed, rod-like and plate-like), but most of the equiaxed UFG neighbors the equiaxed UFG ferrite), as seen in Fig. 2b/d. The total grain area of both ferrite and recovered  $\alpha'$ -martensite (both are indexed as body-centered-cubic in the EBSD analysis) decreases as annealing time increases (Table 2). The grain area of ferrite and recovered  $\alpha'$ -martensite decreases because both UFG ferrite and UFG austenite are generated during intercritical annealing and thus consume

the recovered  $\alpha'$ -martensite. The recovered martensite and ultrafine ferrite respectively constitute approximately 65% and 10% (phase volume fraction) of the microstructure in 8 h condition, while the shorter annealing time (0.5 h) produces approximately 95% recovered martensite and 3% UFG ferrite.

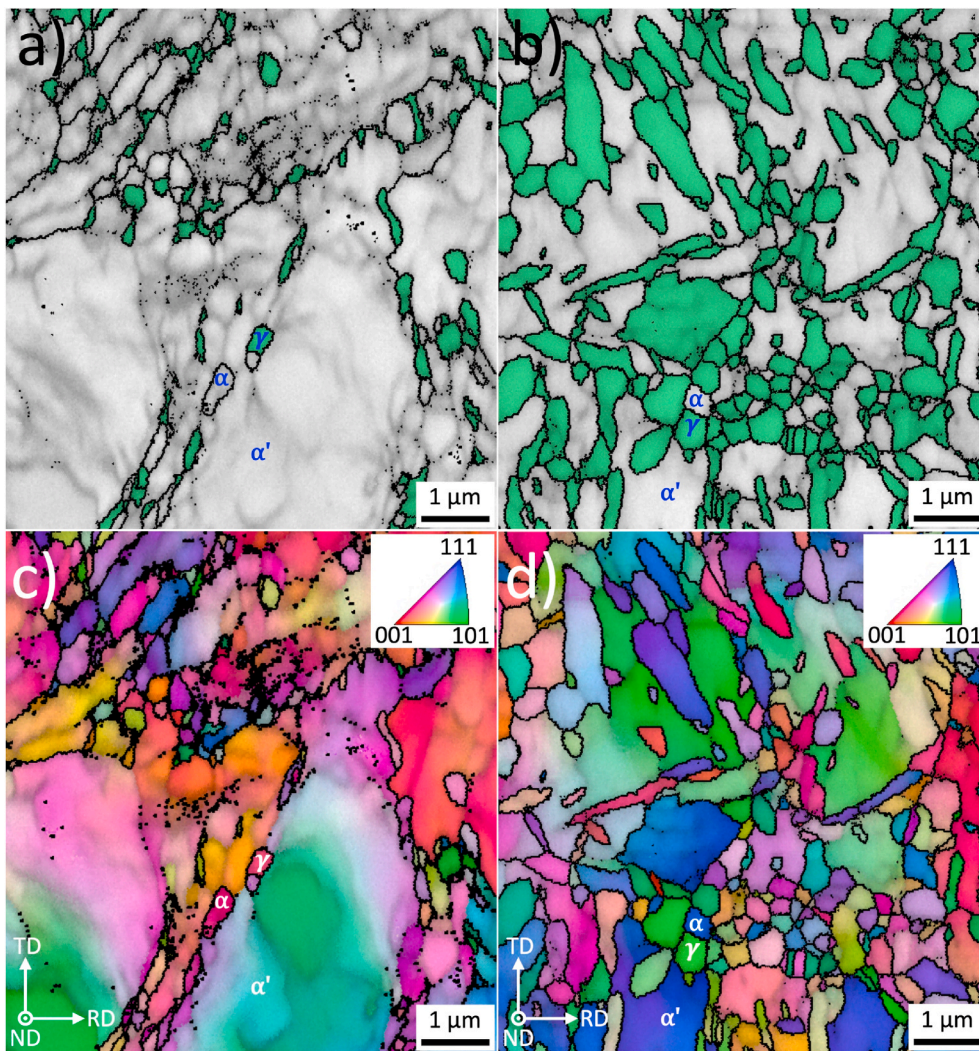
#### 3.2. Non-contact measurements of strain and temperature during servo hydraulic tension tests

Fig. 3a/b shows an engineering stress-strain curve annotated with the optical images used to measure engineering strain with DIC. In all tensile tests and for both heat treatment conditions, DIC does not provide evidence for heterogenous deformation (neither Lüders bands, nor PLC bands). All servo hydraulic tension tests of the 0.5 h heat treated condition are shown in Fig. 3c and labeled according to the nominal intended strain rate. As strain rate increases from  $\dot{\epsilon} = 2 \times 10^{-4} \text{ s}^{-1}$  to  $\dot{\epsilon} = 2 \times 10^{-2} \text{ s}^{-1}$ , the average values of yield strength, UTS and total elongation all increase. Oscillations in engineering stress observed at  $\dot{\epsilon} = 2 \times 10^{-2} \text{ s}^{-1}$  are due to ringing in the load cell and shaking of the tensile specimen.

Fig. 4 shows radiance temperature measurements acquired during servo hydraulic testing. Images and extracted data in Fig. 4a–c are from the same tension test shown in Fig. 3a/b. After 5.5 s of deformation at a strain rate of  $\dot{\epsilon} = 2 \times 10^{-2} \text{ s}^{-1}$ , the maximum temperature of the specimen annealed for 0.5 h is 59 °C (Fig. 4b and c). Thermal imaging during  $\dot{\epsilon} = 2 \times 10^{-2} \text{ s}^{-1}$  tests shows localized heat does not generate until after  $\epsilon_{\text{eng.}} = 0.133$  (after 5.4 s) for the specimen annealed for 0.5 h (Fig. 4a), and is



**Fig. 1.** The electron backscatter diffraction maps of the medium-Mn steel were acquired after cold rolling and intercritical annealing at 585 °C for a) 0.5 h and b) 8 h. The ferrite/ $\alpha'$ -martensite/austenite grain orientations (plus image quality) show minimal signs of recrystallization and reversion after a) 0.5 h at 585 °C, whereas the b) 8 h heat treatment reverts more of the cold-rolled  $\alpha'$ -martensite into ultrafine-grained austenite.



**Fig. 2.** Higher magnification view of the solid boxes outlined in Fig. 1 are presented in two forms: a/b) phase maps (austenite is green) with image quality overlay and defined grain boundaries (black lines), plus c/d) ferrite/ $\alpha'$ -martensite/austenite grain orientations with an image quality overlay. The differences in grain morphology/size and phase fraction of the ultrafine-grained (UFG) austenite, UFG ferrite and remaining recovered  $\alpha'$ -martensite are shown for both annealing times: a/c) 0.5 h and b/d) 8 h. (For interpretation of the references to color in this figure legend, the reader is referred to the Web version of this article.)

**Table 2**

Austenite volume fraction and average grain areas measured with EBSD for the cold-rolled conditions and after intercritical annealing.

Intercritical annealing time (h)	Austenite content (%)	Austenite grain area ( $\mu\text{m}^2$ )	Combined ferrite/ $\alpha'$ -martensite grain area ( $\mu\text{m}^2$ )
0	0	0.005	635
0.5	2	0.073	492
8	35	0.458	79

only due to necking. Consistent with DIC measurements, no static or dynamic strain aging events were observed at any strain rate (true for both annealing times). Necking generated localized heat for all tests and produced a maximum temperature of 110 °C in Fig. 4a ( $\dot{\epsilon}_{\text{eng.}} = 0.173$ , which occurs after the UTS is reached, as shown in Fig. 3a/b). Representative plots of average temperature in the reduced parallel length (excluding the necked region and fracture surface) vs. engineering strain are provided in Fig. 4d. As expected, quasi-static strain rate tests ( $\dot{\epsilon} = 2 \times 10^{-4} \text{ s}^{-1}$ ) produced minimal heating before fracture, while the other strain rates produced minimal heating at best (when considering the average temperature of the non-necked region). As a note, the initial tensile-specimen temperature for  $\dot{\epsilon} = 2 \times 10^1 \text{ s}^{-1}$  tests was greater than other tests since halogen lights were used for this DIC measurement and turned on 30 s prior to the start of the test, whereas test at other strain rates used LED lights. Results from tests at  $\dot{\epsilon} = 2 \times 10^2 \text{ s}^{-1}$  are not

included due to insufficient data acquisition rates of the thermal imaging.

### 3.3. Kolsky bar tension testing

Fig. 5 shows the DIC results and tensile properties from Kolsky bar tension testing of a specimen annealed for 0.5 h and a specimen annealed for 8 h. As seen in Fig. 5d, samples from each annealing condition were deformed to failure at approximately the same strain rate ( $\dot{\epsilon}_{\text{max}} = 1 \times 10^3 \text{ s}^{-1}$ ) with respect to strain. The Kolsky bar engineering stress-strain curves are plotted up until the point of instability (maximum uniform strain) in this case. The oscillations in stress for all Kolsky bar tests are attributed to the impact of the striker bar (the load cell experiences shock waves) and should not be misconstrued as a microstructure-based mechanism. As annealing time increases, the yield strength (YS) decreases by approximately 100 MPa and uniform elongation (UE) increases by 0.07 ( $\epsilon_{\text{eng.}}$ ). Also, the product of UTS and %UE increases by 60% from 10 GPa % to 16 GPa %, which is consistent with results from servo hydraulic testing. Like in servo hydraulic testing, DIC was used to measure strain during all Kolsky bar tensile tests. DIC shows that strain remained relatively uniform (no PLC banding effects were observed) in both specimens, but the specimen annealed for 8 h accommodated a slightly larger area (more necking) of maximum strain (0.35  $\epsilon_{\text{yy}}$  to 0.4  $\epsilon_{\text{yy}}$ ) in the necked region.

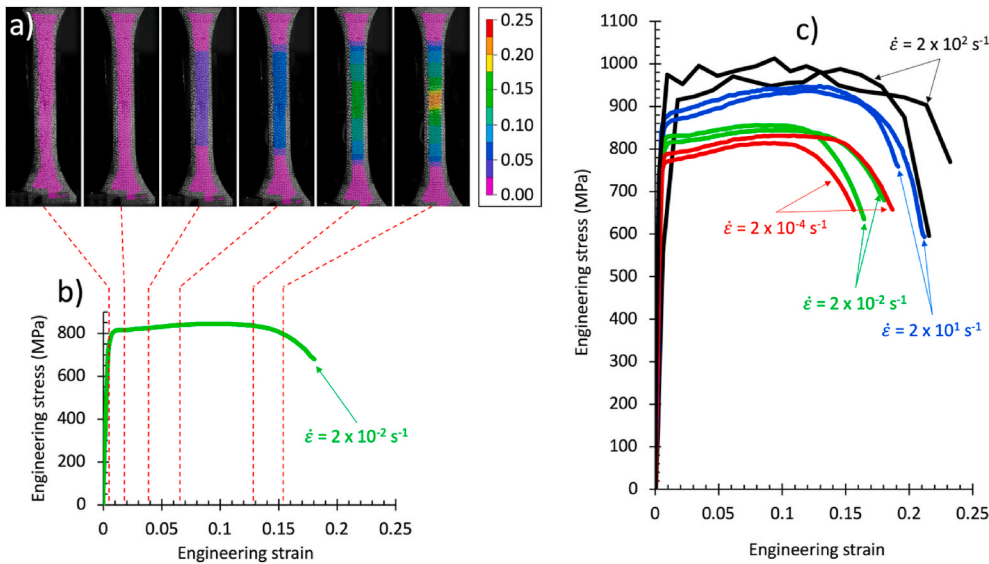


**Fig. 3.** a) Optical images used for digital image correlation provide a non-contact measurement of virtual engineering strain with respect to the tensile direction (color scale provided for  $\epsilon_{yy}$ ) during b) servo hydraulic tension (at  $\dot{\epsilon} = 2 \times 10^{-2} \text{ s}^{-1}$  in this example). The c) engineering stress-strain responses of the medium-Mn steel annealed for 0.5 h are shown for nominal strain rates ranging from  $\dot{\epsilon} = 2 \times 10^{-4} \text{ s}^{-1}$  to  $\dot{\epsilon} = 2 \times 10^2 \text{ s}^{-1}$ . (For interpretation of the references to color in this figure legend, the reader is referred to the Web version of this article.)

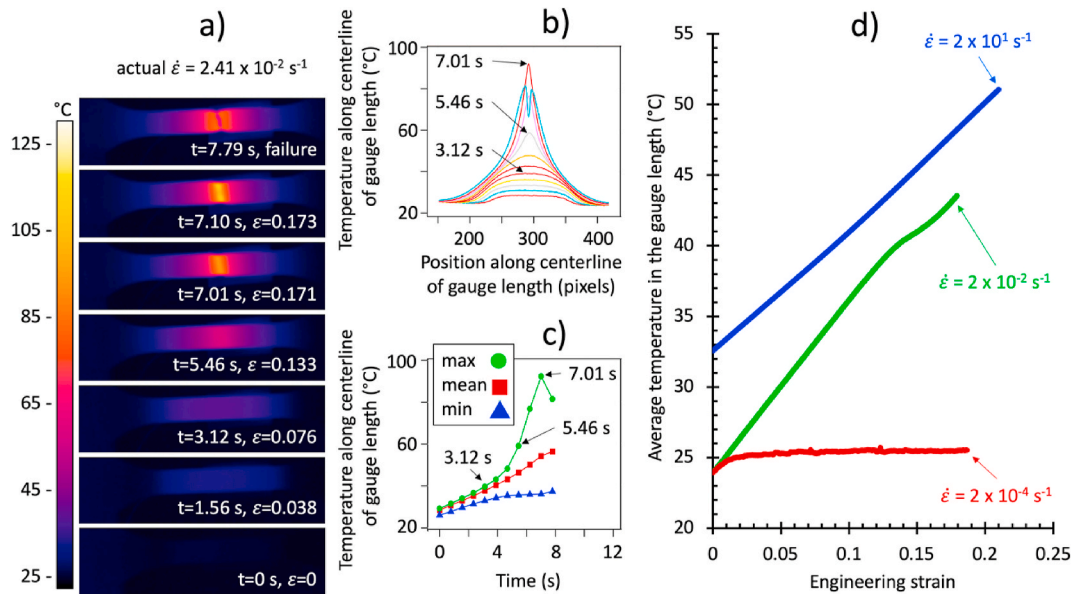


**Fig. 4.** a) Infrared imaging during servo hydraulic tension testing enabled non-contact measurements of radiance temperature (color scale provided for  $^{\circ}\text{C}$ ) as a function of b) position and c) time. Analysis of the infrared images is provided for d) the shorter annealing time (0.5 h), when deformed at strain rates varying from  $\dot{\epsilon} = 2 \times 10^{-4} \text{ s}^{-1}$  to  $\dot{\epsilon} = 2 \times 10^1 \text{ s}^{-1}$ . (For interpretation of the references to color in this figure legend, the reader is referred to the Web version of this article.)

### 3.4. Strain-rate sensitivity via true stress-strain relationships

To provide a comparison between servo hydraulic testing of full-size specimens and Kolsky bar testing of sub-sized tensile specimens, the true stress-strain curves are plotted together, according to heat treatment. All engineering stress-strain curves were converted to true stress-strain curves, following the Considère criterion [1,2]. In Fig. 6, the initial flow stresses measured from Kolsky bar testing ( $\dot{\epsilon} = 9.9 \times 10^2 \text{ s}^{-1}$  and faster) appear greater than those measured from the fastest strain rate achieved with servo hydraulic testing ( $\dot{\epsilon} = 2 \times 10^2 \text{ s}^{-1}$ ). However, enough uncertainty exists in the fastest servo hydraulic tests (due to mechanical vibration of the load cell) such that the YS and thus statistical significance of YS differences (compared to Kolsky bar measurements) was not computed. The UE values measured during Kolsky bar testing of specimens annealed for 8 h fall within the range measured from servo hydraulic testing. The UTS values of all specimens deformed

by Kolsky bar testing are on the order of UTS values measured with servo hydraulic testing at  $\dot{\epsilon} = 2 \times 10^1 \text{ s}^{-1}$  and  $\dot{\epsilon} = 2 \times 10^2 \text{ s}^{-1}$  (for both annealing times).

Strain-rate sensitivities ( $m$  in Equation 1) of the YS are shown in Fig. 7 and based on the actual achieved strain rates (rather than nominal) [43]:

$$\log_{10}(P) = m \bullet \log_{10}(\dot{\epsilon}) + b \tag{1}$$

where,  $P$  is the strength value (YS or UTS),  $m$  is the slope of the linear regression,  $\dot{\epsilon}$  is the strain rate, and  $b$  is the regression intercept. Regressions were completed using two sub-sets of the data (with and without Kolsky bar measurements) and are provided in Table 3 and Table 4. The uncertainties of the strain-rate sensitivities, are expressed as the standard error (see.

Tables 3 and 4). All strain-rate sensitivities presented in Tables 3 and 4 are positive. The YS strain-rate sensitivities that include Kolsky bar

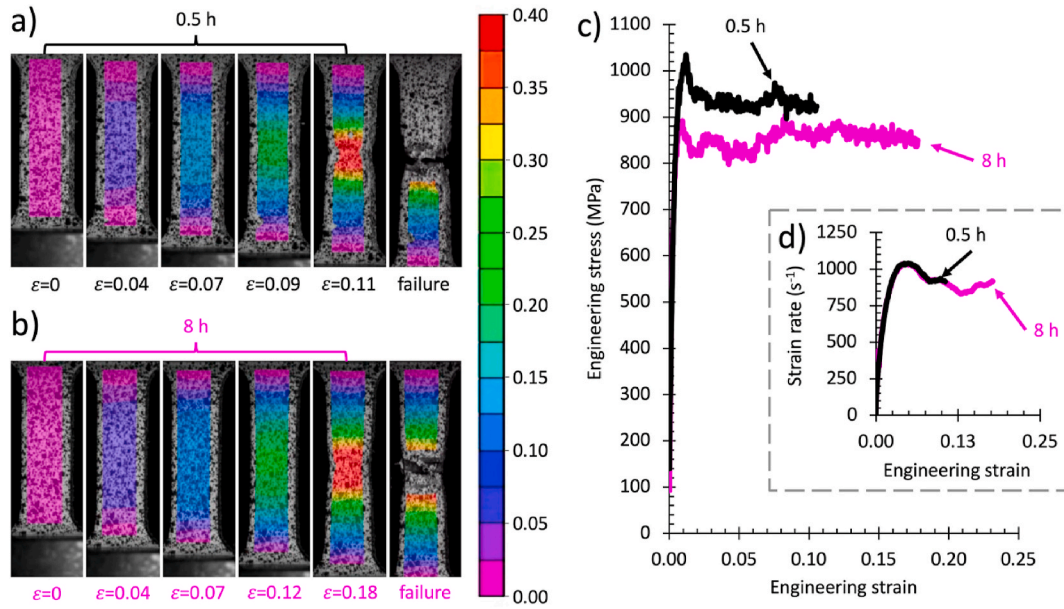


**Fig. 5.** High-speed imaging ( $7.5 \times 10^4$  frames per second) was used to measure engineering strain with digital image correlation (color scale provided for  $\epsilon_{yy}$  where y is the tensile direction) during a/b) Kolsky bar tension at strain rates that exceed  $\dot{\epsilon} = 1 \times 10^3 \text{ s}^{-1}$ . Representative c) engineering stress-strain responses plotted with the same axis limits as Fig. 3d and d) instantaneous strain rates are provided for both annealing times (0.5 h and 8 h). (For interpretation of the references to color in this figure legend, the reader is referred to the Web version of this article.)

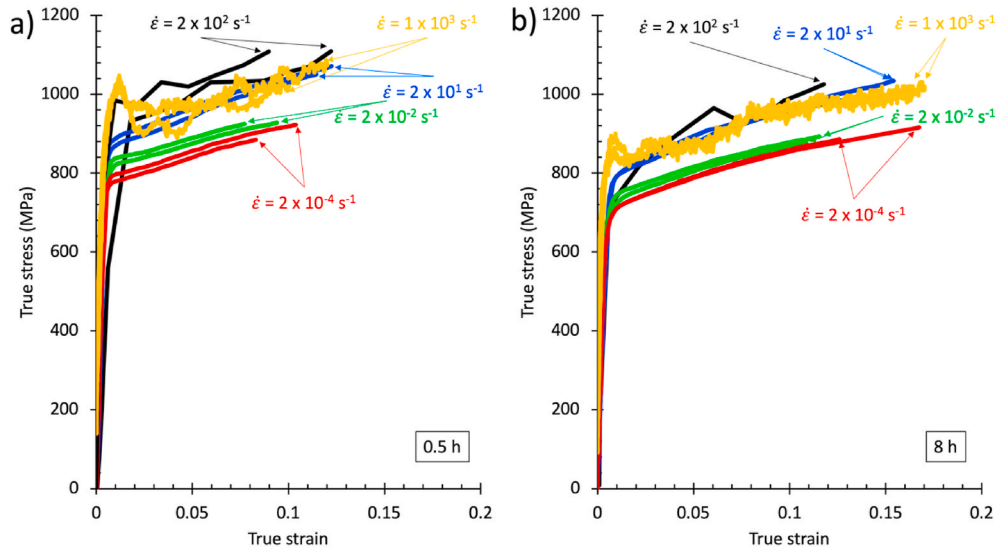


**Fig. 6.** All true stress-strain responses from servo hydraulic tension testing (from  $\dot{\epsilon} = 2 \times 10^{-4} \text{ s}^{-1}$  to  $\dot{\epsilon} = 2 \times 10^2 \text{ s}^{-1}$ ) and Kolsky bar tension testing (from  $\dot{\epsilon} = 9.9 \times 10^2 \text{ s}^{-1}$  to  $\dot{\epsilon} = 1.2 \times 10^3 \text{ s}^{-1}$ ) are shown to compare differences in tensile properties for the a) 0.5 h and b) 8 h annealing times.

measurements are  $m_{YS,0.5 \text{ h,all}} = 0.0157$  (standard error is 0.0011) for the 0.5 h annealing time and  $m_{YS,8 \text{ h,all}} = 0.0159$  (standard error is 0.0014) for the 8 h annealing time. These  $m$  values are both the slopes of the linear fits in Fig. 7a and two of the variables listed in Table 3. When including uncertainties, the difference between  $m_{YS,0.5 \text{ h,all}}$  and  $m_{YS,8 \text{ h,all}}$  is not statistically significant. The YS strain-rate sensitivities of both annealing conditions increase when Kolsky bar measurements are included (servo hydraulic only vs. all data in Table 3) whereas the UTS strain-rate sensitivities decrease after inclusion of Kolsky bar data (Table 4).

The product of UTS (in true stress) and UE (% in true strain) drops slightly from  $\dot{\epsilon} = 2 \times 10^{-4} \text{ s}^{-1}$  to  $\dot{\epsilon} = 2 \times 10^{-2} \text{ s}^{-1}$  for both annealing times (Fig. 7b) mostly from a reduction in UE (the increase in UTS is minimal). The average product of UTS and % UE then increases through strain

rates up to  $\dot{\epsilon} = 2 \times 10^3 \text{ s}^{-1}$  for both annealing times. A comparison between the two annealing times shows the 8 h annealing condition has a greater product of UTS and %UE as compared to the 0.5 h annealing time by approximately 2.5 GPa % (on average) for any given strain rate. The greatest product of UTS (true stress) and %UE (true strain) for the 8 h annealing condition is 17 GPa%. Although many calibration models in literature use true stress-strain information (provided in Fig. 7), the other common practice is to report the product of UTS and % total elongation (TE) using engineering stress-strain values, as opposed to true stress-strain values. As such, the greatest product of UTS (engineering stress) and %TE (engineering strain) for the 8 h annealing condition is 28 GPa %.

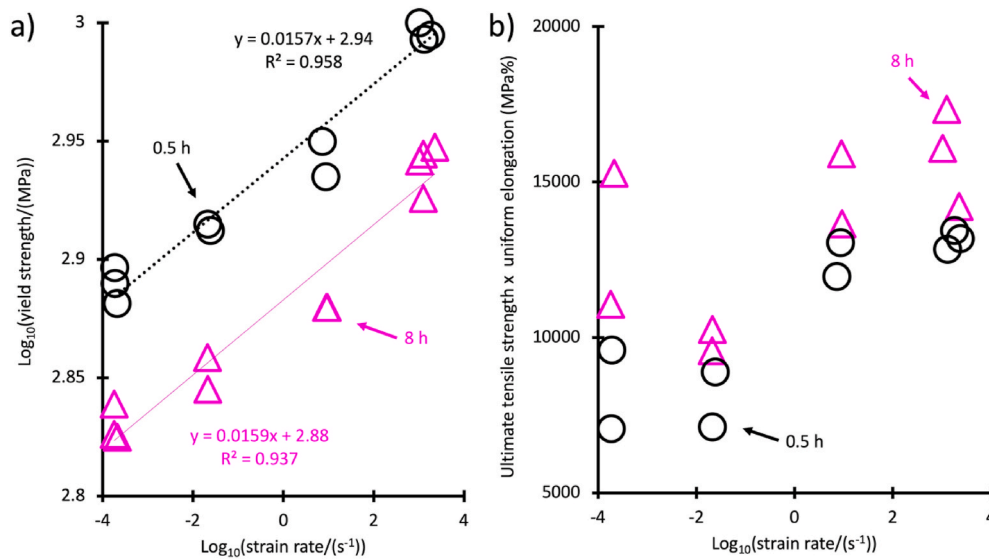


Fig. 7. Comparison between heat treatments for the a) 0.2% offset yield strength strain-rate sensitivity and b) product of ultimate tensile strength (true stress) and uniform elongation (true strain) as a function of achieved strain rate.

**Table 3**  
Strain-rate sensitivity of yield strengths measured for both annealing times.

Annealing time	Testing data used	Variable name	Value of <i>m</i>	Uncertainty of <i>m</i> (standard error)
0.5 h	All data	$m_{YS,0.5 h,all}$	0.0157	0.0011
0.5 h	Servo hydraulic only	$m_{YS,0.5 h,servo}$	0.0115	0.0014
8 h	All data	$m_{YS,8 h,all}$	0.0159	0.0014
8 h	Servo hydraulic only	$m_{YS,8 h,servo}$	0.0106	0.0013

**Table 4**  
Strain-rate sensitivity of ultimate tensile strengths measured for both annealing times.

Annealing time (h)	Testing data used	Variable name	Value of <i>m</i>	Uncertainty of <i>m</i> (standard error)
0.5 h	All data	$m_{UTS,0.5 h,all}$	0.0126	0.0017
0.5 h	Servo hydraulic only	$m_{UTS,0.5 h,servo}$	0.0157	0.0018
8 h	All data	$m_{UTS,8 h,all}$	0.0089	0.0018
8 h	Servo hydraulic only	$m_{UTS,8 h,servo}$	0.0112	0.0031

### 3.5. Fracture behavior

Fig. 8 and Fig. 9 identify fracture surface features in specimens deformed to failure for both annealing conditions. As seen in Figs. 8 and 9, shear lips and micro-void/nano-void coalescence indicate ductile failure, which is representative for specimens deformed at all strain rates and for both heat treatments. Based on analysis of EDS spectra (see supplementary material), the micro-voids likely nucleate near agglomerated particles of Mn sulfides, carbides and/or Al nitrides. However, a unique difference between fracture surface features from different heat treatments is the observation of cleaved regions (Fig. 8a–c) and elongated ledges (Fig. 8d) on fracture surfaces of specimens annealed for 0.5 h. The cleaved regions are flat, approximately 30 μm across, contain features characteristic of cleavage fracture (visible river patterns) and do not show evidence of void coalescence. The elongated ledges are

parallel, lath-like and show no evidence of void coalescence on the inclined surface walls.

## 4. Discussion

### 4.1. Strengthening mechanisms and suppression of plastic instabilities

Intercritical annealing is likely the most important step for determining processing-structure-property relationships in low-C medium-Mn steels. Tuning bulk composition and annealing parameters is paramount when attempting to suppress undesirable plastic instabilities (static and dynamic strain aging effects) by controlling specific microstructural features. Neither heat treatment exhibited static or dynamic strain aging effects (associated with Lüders bands or PLC bands) during mechanical testing, which is discussed in context with the rest of the medium-Mn steel literature. A detailed description of the microstructure is necessary to explain how certain plastic instabilities are suppressed.

During intercritical annealing, the multi-phase microstructure of the cold-rolled Fe–12Mn–3Al–0.05C (% mass fraction) experiences changes in phase fraction and grain size by quantities that span an order-of-magnitude. For example, as annealing time increases from 0.5 h to 8 h, the amount of UFG austenite increases from 2% to 35%, and the average grain area of austenite increases from 0.073 μm<sup>2</sup> to 0.458 μm<sup>2</sup>. To remove effects of strain rate as a variable in this discussion subsection, quasi-static tensile properties are compared to decipher the influence of annealing time on tensile behavior. In addition, it is unlikely that the operable deformation mechanisms in the austenite changed significantly between the two conditions since previous analysis of the austenite compositions [29] identified near equilibrium compositions (meaning the same austenite SFE) for both annealing time. For tensile properties measured at a strain rate of  $\dot{\epsilon} = 2 \times 10^{-4} \text{ s}^{-1}$ , with an increase in annealing time, the YS decreased from 775 MPa to 676 MPa and the UTS decreased from 824 MPa to 780 MPa. The decreases in strength are interpreted to reflect the effects of annealing time on a decrease in α'-martensite phase fraction, decrease in martensite strength due to recovery in the 8 h annealing condition, and correspondingly an increase in the amount and grain size of the UFG austenite and ferrite.

Multiple types of grain morphologies as well as a recovered form of the cold-rolled microstructure were observed after both heat treatments. Many UFG multi-phase medium-Mn steels exhibit effects from Lüders bands [11,32,44–51] and PLC bands [8,19,20]. The mechanisms governing such plastic instabilities are complex. For example, a study by

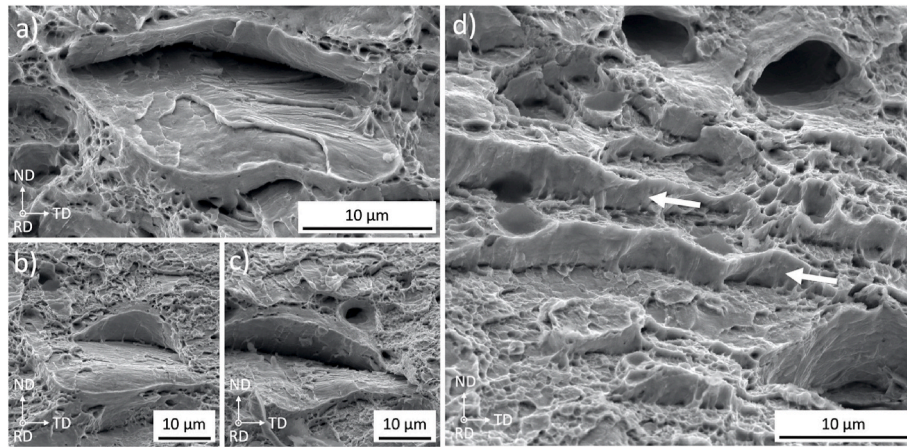


**Fig. 8.** The representative secondary electron images recorded from the center of fracture surfaces of specimens heat treated for 0.5 h and deformed at  $\dot{\epsilon} = 2 \times 10^{-4} \text{ s}^{-1}$  (servo hydraulic tensile specimen geometry) shows instances of a-c) localized cleavage, plus d) lath-like ledges (arrows), and a-d) micro-voids/nano-voids. The rolling direction (RD) is parallel to the direction of tension.

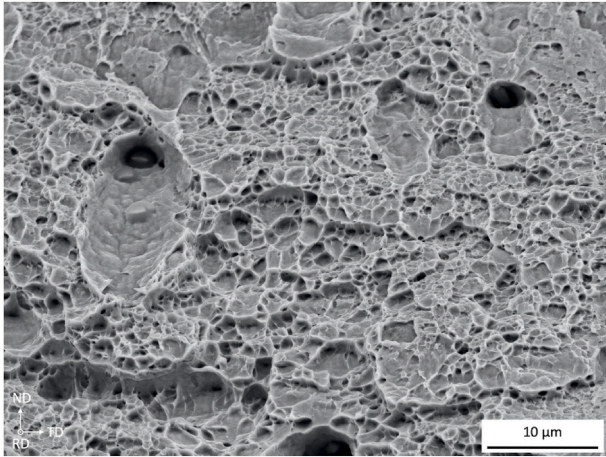


**Fig. 9.** A representative secondary electron image recorded from the center of a fracture surface of a specimen heat treated for 8 h and deformed at  $\dot{\epsilon} = 2 \times 10^{-4} \text{ s}^{-1}$  (servo hydraulic tensile specimen geometry, shows micro-voids, nano-voids and sheared micro-voids). The rolling direction (RD) is parallel to the direction of tension.

Steineder et al. [51] on a cold-rolled Fe-6.4Mn-0.1C (% mass fraction) steel showed that intercritical annealing at 580 °C still produced yield-point elongation after one-step and two-step heat treatments, even though a change in grain morphology was observed (from equiaxed to mostly lamellar with some equiaxed). We attribute the suppression of discontinuous yielding (Lüders banding) to the large fraction and morphology of the recovered martensite, the bimodal-grained microstructure, the fine grain size of ferrite, the multiple austenite morphologies (equiaxed, rod-like and plate-like), and the austenite stability [10, 11, 32, 44–54]. The suppression of PLC bands is most likely due to the morphology of all microstructural constituents, the austenite stability (some TWIP and TRIP effects were observed, but no rapid TRIP effects were evident), and most notably the low carbon content [8, 18–20]. Also, dynamic strain aging events have been shown to occur in medium-Mn steels even after austenite has completed a strain-induced transformation [55]. Suppression of static and dynamic strain aging effects is a formidable challenge when designing complex multi-phase microstructures [54]. The first recommendation for a design strategy that seeks to avoid plastic instabilities/inhomogeneous macro-scale deformation would be to produce a cold-rolled martensitic microstructure with a low-carbon content. The second is to choose an intercritical

annealing temperature at which a SFE of 30 mJ/m<sup>2</sup> or less can be achieved. These recommendations (informed by thermodynamic calculations) for a given medium-Mn steel should produce a multi-phase microstructure with multiple morphologies for short and long annealing times.

#### 4.2. Effects of intercritical annealing time on fracture behavior

The most interesting observations of fracture behavior occur in specimens annealed for 0.5 h and are directly related to the morphology and fraction of the recovered martensite. DIC and thermal imaging showed evidence of necking and ductile failure for both heat-treated conditions and at all strain rates. However, a notable difference between heat treatments in DIC results (using the same specimen geometry) is that the specimens annealed for 8 h accommodate a necking region that is physically larger as well as a greater strain at which necking occurs. Fractography provides evidence of micro-void and nano-void coalescence on the fracture surfaces of specimens deformed at  $\dot{\epsilon} = 2 \times 10^{-4} \text{ s}^{-1}$  for both annealing times (0.5 h and 8 h). There is clear evidence from EDS analysis that micro-voids in this material are nucleated in the vicinity of Mn sulfides, carbides and Al nitrides (supplementary material), even at high strain rates. The presence of carbides, nitrides and inclusions is consistent with the traces of light elements measured from bulk un-deformed specimens (Table 1). Particles, carbides, and Mn-rich austenite embryos that range from 5 nm to 1000 nm in size were identified by means of scanning transmission electron microscopy (STEM) EDS and atom probe tomography (APT) in previous work for samples annealed for 0.5 h at the same temperature [29]. In terms of nano-voids, we believe initiation likely occurs at phase boundaries UFG austenite vs. UFG ferrite/recovered martensite, especially when the strain-induced or stress-assisted martensite transformation intersects a phase boundary [54, 56–59].

In specimens annealed for 0.5 h, flat areas (approximately 30 μm in diameter) showed no signs of void coalescence and contained some river patterns, which are characteristic features of cleavage fracture. The mechanism of this transgranular fracture is typically synonymous with brittle failure. Also, flat facets that are generally about the same size of a ferritic or martensitic constituent are typical indicators of local brittle failure that occurs along a crystallographic plane [60, 61]. Such features also correlate well with the notion that these features were only observed in samples annealed for 0.5 h. Stated plainly, the coarse-grained martensitic constituent in this material condition is a recovered version of the cold-rolled microstructure. It is recognized that effects from rolling still play a key role in the formation of some fracture surface features, highlighted by the orientation of the flat features being

parallel to the rolling direction. The morphology of these features is consistent with planar anisotropy from cold rolling and incomplete recrystallization of the microstructure. These observations are important because brittle failure mechanisms reported for intercritically annealed medium-Mn steels, albeit different mechanisms (quasi-cleavage and intergranular fracture), are typically only associated with hydrogen embrittlement [62–65], low temperature [63,66], or the presence of delta ferrite [67,68], none of which are factors in this work. In the 8 h condition, the total area of the recovered  $\alpha'$ -martensite is more disrupted than in the 0.5 h condition and is likely the reason that such local brittle failures were not observed, even though the recovered  $\alpha'$ -martensite constituted a large fraction of the microstructure. Also, lath-like ledges (no evidence of void coalescence in these regions) were also observed on fracture surfaces of specimens from the 0.5 h annealing treatment and likely originated at lamellar cell block boundaries [56]. Given the multi-phase microstructure and multiple grain sizes in the microstructure, it is reasonable to assume that the coarse-grained parent microstructure dominates the fracture behavior for the material condition produced with a shorter annealing time [69].

#### 4.3. Effects of strain rate on tensile behavior for both annealing times

Positive strain-rate sensitivities of the YS and UTS were measured for both annealing times. Strain-rate sensitivity values ( $m$ ) of the yield strength, measured from  $\dot{\epsilon} = 2 \times 10^{-4} \text{ s}^{-1}$  to  $\dot{\epsilon} = 1 \times 10^3 \text{ s}^{-1}$ , were 0.0157 (standard error is 0.0011) and 0.0159 (standard error is 0.0014) for the 0.5 h and 8 h treatments, respectively. In comparison to other classes of steels, it has been reported that a TRIP800 steel [70] produced an  $m_{YS}$  of 0.0117 across a narrow range of strain rates (from  $\dot{\epsilon} = 8 \times 10^{-2} \text{ s}^{-1}$  to  $\dot{\epsilon} = 2 \times 10^{-1} \text{ s}^{-1}$ ). Also, lower-strength Cr-containing ferritic stainless steels [71] can possess a  $m_{YS}$  ranging from 0.0140 to 0.0210, depending on the range of strain rates measured. Context must also be given to our previous work, which only investigated tensile properties of the 8 h heat treatment [41] and did not include Kolsky-bar tension testing. Tensile properties were measured from  $\dot{\epsilon} = 2 \times 10^{-4} \text{ s}^{-1}$  to  $\dot{\epsilon} = 1 \times 10^1 \text{ s}^{-1}$ , which produced an  $m_{YS}$  of 0.0106. The difference in  $m_{YS}$  (when compared to the current results that include Kolsky-bar tension and high-speed DIC) is statistically significant. These new results are important since the actual strain rates experienced in rapid forming operations and crash-related condition are in excess of  $\dot{\epsilon} = 10^3 \text{ s}^{-1}$  [26–28] and because a positive strain-rate sensitivity can be achieved with a medium-Mn content for both short and long annealing times. Since it has been established that dynamic strain aging leads to negative strain-rate sensitivity [72–74], a positive strain-rate sensitivity coupled with homogeneous macro-scale deformation in a multi-phase steel should generally lead to higher energy absorption in applications where the material experiences high speed deformation.

A multitude of factors are responsible for producing a positive rate sensitivity in a multi-phase steel. Given the suppression of static and dynamic strain aging events, microstructural influences are more easily differentiated by phase and mechanical stability. Although the rate sensitivity exponent is relatively low for UFG (300 nm–1000 nm) face-centered cubic (FCC) and body-centered cubic (BCC) materials [69], the positive strain-rate sensitivity of YS and UTS means time-dependent and thermally activated short-range barriers govern the flow stress [43, 75,76]. As strain rate increases, dislocations have less time to overcome short range obstacles, meaning less time for thermal energy to aid in overcoming such obstacles. In BCC metals, the principal short-range barrier to dislocation motion is the Peierls-Nabarro stress (a friction-based term). In FCC metals, the main short-range barriers to dislocation motion are dislocation forests and solute atoms [77,78]. The differences in short-range barriers when comparing BCC and FCC materials are because the Peierls barrier (measured in energy\*length<sup>-1</sup>) is less energetically favorable (more challenging) to overcome in a BCC lattice (particularly for screw dislocations) as compared to the FCC lattice [75,79]. The major effects on flow stress governing strain-rate

sensitivity in this multi-phase medium-Mn steel are linked to the BCC-based (ferrite and martensite) microstructural constituents, which provides an upper bound on the degree of positive strain-rate sensitivity in a multi-phase steel. This statement is particularly valid for the condition annealed for 0.5 h because only 2% austenite is present in the undeformed state.

Measurements of radiance temperature were necessary to understand and quantify other factors that play a part in the positive strain-rate sensitivity in this multi-phase steel. Even though adiabatic conditions may be met at approximately  $\dot{\epsilon} = 2 \times 10^{-2} \text{ s}^{-1}$ , the limited uniform elongation of this material does not allow for a great amount of thermal softening. Also, the minimal specimen heating does not allow for a large increase in SFE. This is an important point because if enough heat accumulates in the specimen during tension, austenite stability increases due to an increase in SFE. The largest increase in average radiance temperature ( $\Delta T = 25 \text{ }^\circ\text{C}$ ) of the tensile specimen (excluding necking) offers a conservative estimate on the increase in SFE ( $4 \text{ mJ/m}^2$ ) [33,41] and does not produce a notable change in austenitic deformation mechanisms (when the RT SFE is approximately  $21 \text{ mJ/m}^2$ ). While TEM analysis of deformation mechanisms was completed for both annealing times (supplementary material), one must keep in mind that the microstructure in specimens annealed for 0.5 h consists of 2% UFG austenite. Thus, most of the deformation in the 0.5 h condition is accommodated by the rest of the microstructure (dislocation tangles in UFG ferrite and recovered  $\alpha'$ -martensite). To provide more context on the significance of this work (positive UTS strain-rate sensitivity as shown in Table 4), it is noteworthy to mention that a negative UTS strain-rate sensitivity is achieved when deformation mechanisms are strongly influenced by adiabatic heating, i.e. low SFE and/or dynamic strain aging effects in medium-Mn TRIP [28,78,80,81]. In fact, a recent study [82] on strain rate effects for the same nominal steel composition investigated a different intercritical annealing condition (2 h at  $675 \text{ }^\circ\text{C}$  produced 45% UFG austenite with an estimated RT austenite SFE of  $10 \text{ mJ/m}^2$ ). While that study [82] did show a fluctuation in strain-rate sensitivity of the YS and UTS, the overall trend in mechanical properties (based on a comparison of the extremes in strain rate) shows that the product of strength and elongation decreased as strain rate increased.

Finally, Kolsky bar testing of automotive sheet steels provides insight into mechanical property measurements that are relevant to high-speed crash-related conditions and some extreme forming operations. The gauge length of Kolsky bar tensile specimens was less than 1/3 of the reduced parallel length of the servo hydraulic tensile specimens (6.9 mm vs. 25 mm) and the gauge width was approximately half the size (3 mm vs. 6 mm). Kolsky bar DIC results captured at a nominal strain rate of  $\dot{\epsilon} = 1 \times 10^3 \text{ s}^{-1}$  are consistent with servo hydraulic results follow the same trends of servo hydraulic testing where specimens annealed for 8 h have lower YS and UTS values, but greater UE values as compared to specimens annealed for 0.5 h. Moreover, the processing-structure-property relationships presented in this work are unique for medium-Mn steels and show promise for applications which require a material to maintain a positive strain-rate sensitivity of YS and UTS (including moderate uniform elongations and homogenous macro-scale deformation behavior).

## 5. Summary and conclusions

A cold-rolled medium-Mn steel was intercritically annealed with different annealing times at the same temperature, which respectively produced 2% and 35% UFG austenite with variations in morphology. Other microstructural constituents include equiaxed UFG ferrite and coarse-grained recovered  $\alpha'$ -martensite. Strain rate effects were investigated across a large range (from  $\dot{\epsilon} = 2 \times 10^{-4} \text{ s}^{-1}$  to  $\dot{\epsilon} = 1 \times 10^3 \text{ s}^{-1}$ ). Notably, the tensile properties, thermal imaging and digital image correlation measurements provided no evidence of static (Lüders bands) nor dynamic strain-aging (PLC bands) effects for both material

conditions, indicating homogenous deformation behavior on a macroscopic length scale. With the goal of influencing future design strategies, the following conclusions are drawn from this work:

- The suppression of effects from static and dynamic strain aging events is due to a unique combination in size and morphology of the microstructural constituents in this multi-phase material. To achieve this unique microstructure, a low-carbon medium-Mn steel should be cold-rolled and intercritically annealed at a temperature that optimizes phase fraction, grain size, and room temperature austenite stability.
- When comparing the same strain rate, an increase in intercritical annealing time produced a decrease in YS, but an increase in the product of UTS and UE. Most of these changes in mechanical properties per annealing time are due to differences in the size and phase fraction of UFG austenite and recovered martensite.
- The greater phase fraction of the recovered  $\alpha'$ -martensite (a constituent that is present due to an incomplete recrystallization) measured in the shorter annealing time most likely led to localized instances of brittle failure on the fracture surfaces. The flat features (aligned with the rolling direction) in such instances were of the same size and morphology of the coarse-grained  $\alpha'$ -martensite (a recovered form of the cold rolled microstructure).
- When production of a multi-phase medium-Mn steel is optimized, two different material conditions from the same nominal composition can be manufactured to exhibit positive strain-rate sensitivities of the YS, the UTS, and the product of strength and elongation.

#### Data availability

The raw/processed data required to reproduce these findings are available upon request.

#### CRediT authorship contribution statement

**J.T. Benzing:** Conceptualization, Validation, Formal analysis, Investigation, Writing - original draft, Writing - review & editing, Visualization, Project administration. **W.E. Luecke:** Methodology, Validation, Formal analysis, Investigation, Writing - original draft, Writing - review & editing. **S. Mates:** Methodology, Validation, Formal analysis, Investigation, Writing - original draft. **D. Ponge:** Project administration, Investigation, Writing - original draft. **D. Raabe:** Funding acquisition, Supervision, Project administration. **J.E. Wittig:** Funding acquisition, Supervision, Project administration, Methodology.

#### Declaration of competing interest

The authors declare that they have no known competing financial interests or personal relationships that could have appeared to influence the work reported in this paper.

#### Acknowledgements

This work was partially funded by the United States National Science Foundation (US-NSF) Division of Materials Research under grant DMR1309258, US-NSF EPS 1004083 and the Max Planck Institute für Eisenforschung in Düsseldorf, Germany. Servo hydraulic tension testing, Kolsky bar tension testing, digital image correlation and thermal imaging were all completed in the Center for Automotive Lightweighting (NCAL) at the National Institute of Standards and Technology in Gaithersburg, MD.

#### Appendix A. Supplementary data

Supplementary data to this article can be found online at <https://doi.org/10.1016/j.msea.2020.140469>.

#### References

- [1] D.K. Matlock, J.G. Speer, Processing opportunities for new advanced high-strength sheet steels, *Mater. Manuf. Process.* 25 (2010) 1–3, <https://doi.org/10.1080/10426910903158272>, 7–13.
- [2] D.K. Matlock, J.G. Speer, Third generation of AHSS: microstructure design concepts, in: A. Haldar, S. Suwas, D. Bhattacharjee (Eds.), *Microstruct. Texture Steels*, Springer, London, 2009, pp. 185–205, [https://doi.org/10.1007/978-1-84882-454-6\\_11](https://doi.org/10.1007/978-1-84882-454-6_11).
- [3] D.T. Pierce, J.A. Jiménez, J. Bentley, D. Raabe, J.E. Wittig, The influence of stacking fault energy on the microstructural and strain-hardening evolution of Fe-Mn-Al-Si steels during tensile deformation, *Acta Mater.* 100 (2015) 178–190, <https://doi.org/10.1016/j.actamat.2015.08.030>.
- [4] D.R. Steinmetz, T. Jäpel, B. Wietbrock, P. Eisenlohr, I. Gutierrez-Urrutia, A. Saeed-Akbari, T. Hickel, F. Roters, D. Raabe, Revealing the strain-hardening behavior of twinning-induced plasticity steels: theory, simulations, experiments, *Acta Mater.* 61 (2013) 494–510, <https://doi.org/10.1016/j.actamat.2012.09.064>.
- [5] I. Gutierrez-Urrutia, S. Zaeferrer, D. Raabe, The effect of grain size and grain orientation on deformation twinning in a Fe-22wt.% Mn-0.6wt.% C TWIP steel, *Mater. Sci. Eng.* 527 (2010) 3552–3560, <https://doi.org/10.1016/j.msea.2010.02.041>.
- [6] F.B. Pickering, *Toward Improved Toughness and Ductility, Climax Molybdenum Dev. Co.*, 1971, pp. 9–32.
- [7] D.K. Matlock, G. Krauss, F. Zia-Ebrahimi, *Deformation, Processing and Structure, ASM, Met. Park. OH*, 1984, pp. 47–87.
- [8] D.M. Field, J. Qing, D.C. van Aken, Chemistry and properties of medium-Mn two-stage TRIP steels, *Metall. Mater. Trans. A Phys. Metall. Mater. Sci.* (2018) 1–18, <https://doi.org/10.1007/s11661-018-4798-6>.
- [9] Y.-K. Lee, J. Han, Current opinion in medium manganese steel, *Mater. Sci. Technol.* 31 (2015) 843–856, <https://doi.org/10.1179/1743284714Y.0000000722>.
- [10] F. Yang, H. Luo, C. Hu, E. Pu, H. Dong, Effects of intercritical annealing process on microstructures and tensile properties of cold-rolled 7Mn steel, *Mater. Sci. Eng.* 685 (2017) 115–122, <https://doi.org/10.1016/j.msea.2016.12.119>.
- [11] Y. Ma, W. Song, S. Zhou, A. Schwedt, W. Bleck, Influence of intercritical annealing temperature on microstructure and mechanical properties of a cold-rolled medium-Mn steel, *Metals* 8 (2018) 357, <https://doi.org/10.3390/met8050357>.
- [12] S. Lee, B.C. De Cooman, On the selection of the optimal intercritical annealing temperature for medium Mn TRIP steel, *Metall. Mater. Trans.* 44 (2013) 5018–5024, <https://doi.org/10.1007/s11661-013-1860-2>.
- [13] S. Lee, K. Lee, B.C. de Cooman, Observation of the TWIP + TRIP plasticity-enhancement mechanism in Al-added 6 Wt pct medium Mn steel, *Metall. Mater. Trans.* (2015) 1–8, <https://doi.org/10.1007/s11661-015-2854-z>.
- [14] S. Lee, W. Woo, B.C. de Cooman, Analysis of the tensile behavior of 12 pct Mn multi-phase ( $\alpha + \gamma$ ) TWIP + TRIP steel by neutron diffraction, *Metall. Mater. Trans.* 47 (2016) 2125–2140, <https://doi.org/10.1007/s11661-016-3407-9>.
- [15] C. Wang, W. Cao, J. Shi, C. Huang, H. Dong, Deformation microstructures and strengthening mechanisms of an ultrafine grained duplex medium-Mn steel, *Mater. Sci. Eng.* 562 (2013) 89–95, <https://doi.org/10.1016/j.msea.2012.11.044>.
- [16] R. Zhang, W.Q. Cao, Z.J. Peng, J. Shi, H. Dong, C.X. Huang, Intercritical rolling induced ultra fine microstructure and excellent mechanical properties of the medium-Mn steel, *Mater. Sci. Eng.* 583 (2013) 84–88, <https://doi.org/10.1016/j.msea.2013.06.067>.
- [17] M.C. McGrath, D.C. Van Aken, N.I. Medvedeva, J.E. Medvedeva, Work hardening behavior in steel with multiple TRIP mechanisms, *Metall. Mater. Trans.* 44 (2013) 4634–4643, <https://doi.org/10.1007/s11661-013-1820-x>.
- [18] S.J. Lee, J. Kim, S.N. Kane, B.C. De Cooman, On the origin of dynamic strain aging in twinning-induced plasticity steels, *Acta Mater.* 59 (2011) 6809–6819, <https://doi.org/10.1016/j.actamat.2011.07.040>.
- [19] M. Callahan, O. Hubert, F. Hild, A. Perlade, J.H. Schmitt, Coincidence of strain-induced TRIP and propagative PLC bands in Medium Mn steels, *Mater. Sci. Eng.* 704 (2017) 391–400, <https://doi.org/10.1016/j.msea.2017.08.042>.
- [20] Y. Zhang, L. Wang, K.O. Findley, J.G. Speer, Influence of temperature and grain size on austenite stability in medium manganese steels, *Metall. Mater. Trans.* 48 (2017) 2140–2149, <https://doi.org/10.1007/s11661-017-3995-z>.
- [21] J. Hu, J.M. Zhang, G.S. Sun, L.X. Du, Y. Liu, Y. Dong, R.D.K. Misra, High strength and ductility combination in nano-/ultrafine-grained medium-Mn steel by tuning the stability of reverted austenite involving intercritical annealing, *J. Mater. Sci.* 54 (2019) 6565–6578, <https://doi.org/10.1007/s10853-018-03291-w>.
- [22] R. Rana, E. De Moor, J.G. Speer, D.K. Matlock, Effects of hot band Annealing on the mechanical properties of cold-rolled and intercritically annealed medium manganese steels, *Metall. Mater. Trans.* 50 (2019) 4016–4020, <https://doi.org/10.1007/s11661-019-05363-1>.
- [23] D.M. Field, D.C. Van Aken, Dynamic strain aging phenomena and tensile response of medium-Mn TRIP steel, *Metall. Mater. Trans.* 49 (2018) 1152–1166, <https://doi.org/10.1007/s11661-018-4481-y>.
- [24] L. Chen, J. Kim, S.K. Kim, K.G. Chin, B.C. De Cooman, On the stretch-flangeability of high Mn TWIP steels, *Mater. Sci. Forum* 654–656 (2010) 278–281, <https://doi.org/10.4028/www.scientific.net/MSF.654-656.278>.
- [25] L. Xu, L. Chen, B.C. de Cooman, D. Steglich, F. Barlat, Hole expansion of advanced high strength steel sheet sample, *Int. J. Material Form.* 3 (2010) 247–250, <https://doi.org/10.1007/s12289-010-0753-9>.
- [26] M. Seth, V.J. Vohnout, G.S. Daehn, Formability of steel sheet in high velocity impact, *J. Mater. Process. Technol.* 168 (2005) 390–400, <https://doi.org/10.1016/j.jmatprotec.2004.08.032>.
- [27] S. Hiermaier, *Structures under Crash and Impact: Continuum Mechanics, Discretization and Experimental Characterization*, New York, 2008.

- [28] R. Alturk, L.G.H. Jr, C.M. Enloe, F. Abu-farha, T.W. Brown, Strain rate effect on tensile flow behavior and anisotropy of a medium-manganese TRIP steel, *J. Occup. Med.* 70 (2018) 894–905, <https://doi.org/10.1007/s11837-018-2830-3>.
- [29] J.T. Benzing, A. Kwiatkowski da Silva, L. Morsdorf, J. Bentley, D. Ponge, A. Dutta, J. Han, J.R. McBride, B. Van Leer, B. Gault, D. Raabe, J.E. Wittig, Multi-scale characterization of austenite reversion and martensite recovery in a cold-rolled medium-Mn steel, *Acta Mater.* 166 (2019) 512–530, <https://doi.org/10.1016/j.actamat.2019.01.003>.
- [30] D.T. Pierce, J.A. Jimenez, J. Bentley, D. Raabe, C. Oskay, J.E. Wittig, The influence of manganese content on the stacking fault and austenite/epsilon-martensite interfacial energies in Fe-Mn-(Al-Si) steels investigated by experiment and theory, *Acta Mater.* 68 (2014) 238–253, <https://doi.org/10.1016/j.actamat.2014.01.001>.
- [31] M. Pozuelo, J.E. Wittig, J.A. Jiménez, G. Frommeyer, Enhanced mechanical properties of a novel high-nitrogen Cr-Mn-Ni-Si austenitic stainless steel via TWIP/TRIP effects, *Metall. Mater. Trans. A Phys. Metall. Mater. Sci.* 40 (2009) 1826–1834, <https://doi.org/10.1007/s11661-009-9863-8>.
- [32] Y. Ma, Medium-manganese steels processed by austenite-reverted-transformation annealing for automotive applications, *Mater. Sci. Technol.* 33 (2017) 1713–1727, <https://doi.org/10.1080/02670836.2017.1312208>.
- [33] J.T. Benzing, W.A. Poling, D.T. Pierce, J. Bentley, K.O. Findley, D. Raabe, J. E. Wittig, Effects of strain rate on mechanical properties and deformation behavior of an austenitic Fe-25Mn-3Al-3Si TWIP-TRIP steel, *Mater. Sci. Eng.* 711 (2018) 78–92, <https://doi.org/10.1016/j.msea.2017.11.017>.
- [34] J.T. Benzing, J.E. Wittig, T.M. Smith, M.J. Mills, J.R. Johnson, G.S. Daehn, J. Bentley, D. Raabe, C. Ophus, Fe-25Mn-3Al-3Si TWIP-TRIP steel deformed at high strain-rates, *Microsc. Microanal.* 21 (Suppl 3) (2015) 1745–1746, <https://doi.org/10.1017/S1431927615009502>.
- [35] J.T. Benzing, J. Bentley, W. Poling, K. Findley, D.T. Pierce, J.M. Sosa, H.L. Fraser, D. Raabe, J.E. Wittig, Microstructural characterization of a Fe-25Mn-3Al-3Si TWIP-TRIP steel, *Microsc. Microanal.* 22 (Suppl 3) (2016) 1962–1963, <https://doi.org/10.1017/S1431927616010655>.
- [36] S. Curtze, V.T. Kuokkala, Dependence of tensile deformation behavior of TWIP steels on stacking fault energy, temperature and strain rate, *Acta Mater.* 58 (2010) 5129–5141, <https://doi.org/10.1016/j.actamat.2010.05.049>.
- [37] O. Grässel, G. Frommeyer, C. Derder, H. Hofmann, Phase transformations and mechanical properties of Fe-Mn-Si-Al TRIP-steels, *J. Phys. IV* 7 (1997) 383–388, <https://doi.org/10.1051/jp4:1997560>.
- [38] S. Allain, J.P. Chateau, O. Bouaziz, S. Migot, N. Guelton, Correlations between the calculated stacking fault energy and the plasticity mechanisms in Fe-Mn-C alloys, *Mater. Sci. Eng.* 387–389 (2004) 158–162, <https://doi.org/10.1016/j.msea.2004.01.059>.
- [39] A. Dumay, J.P. Chateau, S. Allain, S. Migot, O. Bouaziz, Influence of addition elements on the stacking-fault energy and mechanical properties of an austenitic Fe-Mn-C steel, *Mater. Sci. Eng.* 483–484 (2008) 184–187, <https://doi.org/10.1016/j.msea.2006.12.170>.
- [40] A. Saeed-Akbari, J. Imlau, U. Prahll, W. Bleck, Derivation and variation in composition-dependent stacking fault energy maps based on subregular solution model in high-manganese steels, *Metall. Mater. Trans. A Phys. Metall. Mater. Sci.* 40 (2009) 3076–3090, <https://doi.org/10.1007/s11661-009-0050-8>.
- [41] J.T. Benzing, Y. Liu, X. Zhang, W.E. Luecke, D. Ponge, A. Dutta, C. Oskay, D. Raabe, J.E. Wittig, Experimental and numerical study of mechanical properties of multi-phase medium-Mn TWIP-TRIP steel: influences of strain rate and phase constituents, *Acta Mater.* 177 (2019) 250–265, <https://doi.org/10.1016/j.actamat.2019.07.036>.
- [42] O. Guzman, D.J. Frew, W. Chen, A Kolsky tension bar technique using a hollow incident tube, *Meas. Sci. Technol.* (2011), <https://doi.org/10.1088/0957-0233/22/4/045703>.
- [43] G.E. Dieter, *Mechanical Metallurgy*, Page 297, third ed., McGraw-Hill, Boston, 1986.
- [44] R.L. Miller, Ultrafine-grained microstructures and mechanical properties of alloy steels, *Metall. Trans.* 3 (1972) 905–912, <https://doi.org/10.1007/BF02647665>.
- [45] S. Lee, S.J. Lee, S. Santhosh Kumar, K. Lee, B.C.D. Cooman, Localized deformation in multiphase, ultra-fine-grained 6 Pct Mn transformation-induced plasticity steel, *Metall. Mater. Trans.* 42 (2011) 3638–3651, <https://doi.org/10.1007/s11661-011-0636-9>.
- [46] J. Han, S.H. Kang, S.J. Lee, Y.K. Lee, Fabrication of bimodal-grained Al-free medium Mn steel by double intercritical annealing and its tensile properties, *J. Alloys Compd.* 681 (2016) 580–588, <https://doi.org/10.1016/j.jallcom.2016.04.014>.
- [47] B.C. De Cooman, P. Gibbs, S. Lee, D.K. Matlock, Transmission electron microscopy analysis of yielding in ultrafine-grained medium Mn transformation-induced plasticity steel, *Metall. Mater. Trans.* 44 (2013) 2563–2572, <https://doi.org/10.1007/s11661-013-1638-6>.
- [48] P.J. Gibbs, B.C. De Cooman, D.W. Brown, B. Clausen, J.G. Schroth, M.J. Merwin, D. K. Matlock, Strain partitioning in ultra-fine grained medium-manganese transformation induced plasticity steel, *Mater. Sci. Eng.* 609 (2014) 323–333, <https://doi.org/10.1016/j.msea.2014.03.120>.
- [49] J. Chen, M. Lv, S. Tang, Z. Liu, G. Wang, Correlation between mechanical properties and retained austenite characteristics in a low-carbon medium manganese alloyed steel plate, *Mater. Char.* 106 (2015) 108–111, <https://doi.org/10.1016/j.matchar.2015.05.026>.
- [50] B. Sun, Y. Ma, N. Vanderesse, R.S. Varanasi, W. Song, P. Bocher, D. Ponge, D. Raabe, Macroscopic to nanoscopic in situ investigation on yielding mechanisms in ultrafine grained medium Mn steels: role of the austenite-ferrite interface, *Acta Mater.* 178 (2019) 10–25, <https://doi.org/10.1016/j.actamat.2019.07.043>.
- [51] K. Steineder, D. Krizan, R. Schneider, C. Béal, C. Sommitsch, On the microstructural characteristics influencing the yielding behavior of ultra-fine grained medium-Mn steels, *Acta Mater.* 139 (2017) 39–50, <https://doi.org/10.1016/j.actamat.2017.07.056>.
- [52] J. Han, A.K. da Silva, D. Ponge, D. Raabe, S.M. Lee, Y.K. Lee, S.I. Lee, B. Hwang, The effects of prior austenite grain boundaries and microstructural morphology on the impact toughness of intercritically annealed medium Mn steel, *Acta Mater.* 122 (2017) 199–206, <https://doi.org/10.1016/j.actamat.2016.09.048>.
- [53] J. Han, S.-J. Lee, J.-G. Jung, Y.-K. Lee, The effects of the initial martensite microstructure on the microstructure and tensile properties of intercritically annealed Fe-9Mn-0.05C steel, *Acta Mater.* 78 (2014) 369–377.
- [54] D. Raabe, B. Sun, A. Kwiatkowski Da Silva, B. Gault, H.W. Yen, K. Sedighiani, P. Thoudden Sukumar, I.R. Souza Filho, S. Katnagalla, E. Jäggle, P. Kürsteiner, N. Kusampudi, L. Stephenson, M. Herbig, C.H. Liebscher, H. Springer, S. Zaefferer, V. Shah, S.L. Wong, C. Baron, M. Diehl, F. Roters, D. Ponge, Current challenges and opportunities in microstructure-related properties of advanced high-strength steels, *Metall. Mater. Trans. A Phys. Metall. Mater. Sci.* (2020), <https://doi.org/10.1007/s11661-020-05947-2>.
- [55] B. Sun, N. Vanderesse, F. Fazeli, C. Scott, J. Chen, P. Bocher, M. Jahazi, S. Yue, Discontinuous strain-induced martensite transformation related to the Portevin-Le Chatelier effect in a medium manganese steel, *Scripta Mater.* 133 (2017) 9–13, <https://doi.org/10.1016/j.scriptamat.2017.01.022>.
- [56] P. Noell, J. Carroll, K. Hattar, B. Clark, B. Boyce, Do voids nucleate at grain boundaries during ductile rupture? *Acta Mater.* 137 (2017) 103–114, <https://doi.org/10.1016/j.actamat.2017.07.004>.
- [57] Z.H. Cai, H.Y. Li, S.Y. Jing, Z.C. Li, H. Ding, Z.Y. Tang, R.D.K. Misra, Influence of annealing temperature on microstructure and tensile property of cold-rolled Fe-0.2C-11Mn-6Al steel, *Mater. Char.* 137 (2018) 256–262, <https://doi.org/10.1016/j.matchar.2018.01.043>.
- [58] M.M. Wang, C.C. Tasan, D. Ponge, A.C. Dippel, D. Raabe, Nanolaminate transformation-induced plasticity-twinning-induced plasticity steel with dynamic strain partitioning and enhanced damage resistance, *Acta Mater.* 85 (2015) 216–228, <https://doi.org/10.1016/j.actamat.2014.11.010>.
- [59] A. Pineau, A.A. Benzerga, T. Pardoen, Failure of metals I: brittle and ductile fracture, *Acta Mater.* 107 (2016) 424–483, <https://doi.org/10.1016/j.actamat.2015.12.034>.
- [60] G.E. Dieter, *Mechanical Metallurgy*, third ed., McGraw-Hill, Boston, 1986.
- [61] R.W. Hertzberg, Deformation and Fracture Mechanics of Engineering Materials, 1996, p. 810, [https://doi.org/10.1016/0261-3069\(84\)90070-0](https://doi.org/10.1016/0261-3069(84)90070-0).
- [62] X. Shen, W. Song, S. Sevsek, Y. Ma, C. Hüter, R. Spatschek, W. Bleck, Influence of microstructural morphology on hydrogen embrittlement in a medium-Mn steel Fe-12Mn-3Al-0.05C, *Metals* 9 (2019) 929, <https://doi.org/10.3390/met9090929>.
- [63] J. Han, J.H. Nam, Y.K. Lee, The mechanism of hydrogen embrittlement in intercritically annealed medium Mn TRIP steel, *Acta Mater.* 113 (2016) 1–10, <https://doi.org/10.1016/j.actamat.2016.04.038>.
- [64] B.C. Cameron, M. Koyama, C.C. Tasan, Phase stability effects on hydrogen embrittlement resistance in martensite-reverted austenite steels, *Metall. Mater. Trans.* 50 (2018) 1–6, <https://doi.org/10.1007/s11661-018-4948-x>.
- [65] M. Wang, C.C. Tasan, M. Koyama, D. Ponge, D. Raabe, Enhancing hydrogen embrittlement resistance of lath martensite by introducing nano-films of interlath austenite, *Metall. Mater. Trans.* 46 (2015) 3797–3802, <https://doi.org/10.1007/s11661-015-3009-y>.
- [66] M. Madivala, A. Schwedt, S. Leen, F. Roters, U. Prahll, W. Bleck, Temperature dependent strain hardening and fracture behavior of TWIP steel, *Int. J. Plast.* 104 (2018) 80–103, <https://doi.org/10.1016/j.ijplas.2018.02.001>.
- [67] S. Lee, S.H. Kang, J.H. Nam, S.M. Lee, J.B. Seol, Y.K. Lee, Effect of tempering on the microstructure and tensile properties of a martensitic medium-Mn lightweight steel, *Metall. Mater. Trans. A Phys. Metall. Mater. Sci.* 50 (2019) 2655–2664, <https://doi.org/10.1007/s11661-019-05190-4>.
- [68] B. Sun, D. Palanisamy, D. Ponge, B. Gault, F. Fazeli, C. Scott, S. Yue, D. Raabe, Revealing fracture mechanisms of medium manganese steels with and without delta-ferrite, *Acta Mater.* 164 (2019) 683–696, <https://doi.org/10.1016/j.actamat.2018.11.029>.
- [69] A. Pineau, A. Amine Benzerga, T. Pardoen, Failure of metals III: fracture and fatigue of nanostructured metallic materials, *Acta Mater.* 107 (2016) 508–544, <https://doi.org/10.1016/j.actamat.2015.07.049>.
- [70] F. Ozturk, A. Polat, S. Toros, R.C. Picu, Strain hardening and strain rate sensitivity behaviors of advanced high strength steels, *J. Iron Steel Res. Int.* 20 (2013) 68–74, [https://doi.org/10.1016/S1006-706X\(13\)60114-4](https://doi.org/10.1016/S1006-706X(13)60114-4).
- [71] K.D. Clarke, R.J. Comstock, M.C. Mataya, C.J. Tyne, D.K. Matlock, Effect of strain rate on the yield stress of ferritic stainless steels, *Metall. Mater. Trans. A Phys. Metall. Mater. Sci.* 39 (A) (2008) 752–762, <https://doi.org/10.1007/s11661-008-9479-4>.
- [72] A. Benallal, T. Borvik, A. Clausen, O. Hopperstad, Dynamic Strain Aging, Negative Strain-Rate Sensitivity and Related Instabilities  $\sigma$  s s e r t e r P l a s t i c s t r a i n e
- [73] B.A. Wilcox, A.R. Rosenfield, On serrated yielding and negative on strain-rate sensitivity, *Chem. Eng. J.* 1 (1970) 83–84, [https://doi.org/10.1016/0300-9467\(70\)85035-3](https://doi.org/10.1016/0300-9467(70)85035-3).
- [74] R.A. Mulford, U.F. Kocks, New observations ON the mechanisms OF dynamic strain aging and OF jerky flow, *Acta Metall.* 27 (1979) 1125–1134.
- [75] D. Hull, D.J. Bacon, *Introduction to Dislocations*, fifth ed., Butterworth-Heinemann, 2011.
- [76] M.A. Meyers, *Dynamic Behavior of Materials* (1994), <https://doi.org/10.1007/s11340-012-9598-0>.

- [77] G.T. Rusty, Gray, High-strain-rate deformation: mechanical behavior and deformation substructures induced, *Annu. Rev. Mater. Res.* 42 (2012) 285–303, <https://doi.org/10.1146/annurev-matsci-070511-155034>.
- [78] W. Poling, *Tensile Deformation of Third Generation Advanced High Strength Sheet Steels under High Strain Rates*, Colorado School of Mines, 2016. Ph.D. dissertation.
- [79] S. Lee, S.J. Lee, B.C. De Cooman, Work hardening behavior of ultrafine-grained Mn transformation-induced plasticity steel, *Acta Mater.* 59 (2011) 7546–7553, <https://doi.org/10.1016/j.actamat.2011.08.030>.
- [80] R. Rana, E. de Moor, J.G. Speer, D.K. Matlock, On the importance of adiabatic heating on deformation behavior of medium-manganese sheet steels, *JOM (J. Occup. Med.)* (2018) 1–8, <https://doi.org/10.1007/s11837-018-2779-2>.
- [81] M.H. Cai, W.J. Zhu, N. Stanford, L.B. Pan, Q. Chao, P.D. Hodgson, Dependence of deformation behavior on grain size and strain rate in an ultrahigh strength-ductile Mn-based TRIP alloy, *Mater. Sci. Eng.* 653 (2016) 35–42, <https://doi.org/10.1016/j.msea.2015.11.103>.
- [82] S. Sevsek, C. Haase, W. Bleck, Strain-rate-dependent deformation behavior and mechanical properties of a multi-phase medium-manganese steel, *Metals* 9 (2019), <https://doi.org/10.3390/met9030344>.